# Dynamical response of magnetic tubes to transverse perturbations

## I. Thick flux tubes

**U. Ziegler and P. Ulmschneider**

Institut für Theoretische Astrophysik der Universität Heidelberg, Tiergartenstr. 15, D-69121 Heidelberg, Germany

**Abstract.** By means of a 3D numerical code we investigate the response of magnetic flux tubes to transverse perturbations. Various tubes with plasma $\beta$ ranging from 0.1 to 10 embedded in a uniform nonmagnetic atmosphere are considered. High spatial resolution was obtained by the application of a multiple nested grid strategy. Various kinds of internal longitudinal and transverse body waves as well as surface waves were found in addition to the external sound wave.

A great advantage of our 3D treatment is that it allows to treat energy leakage and mode conversion. We investigated the efficiency of wave energy leakage from the magnetic tube to the external medium and found leakage rates ranging from 0.07 for the $\beta = 10$ tube to 0.43 for the $\beta = 0.1$ tube. This shows that leakage is an important process particularly for low $\beta$ tubes and should not be ignored in studies of transverse wave propagation.

As already found in 1D calculations, the purely transverse excitation generates longitudinal body waves of twice the frequency. This mode conversion process is not very efficient. A very important result of our computations, however, is the efficient generation of a non-axisymmetric longitudinal body wave which does not derive from magnetic tension forces, but is due to an inertial pile-up effect inside the tube produced by the transverse motions. Particularly in low $\beta$-tubes, the mode conversion rate for the longitudinal waves was found to be as large as 90% of the total kinetic tube energy most of it is going into the surface wave. This may be very significant for the heating of flux tubes and thus for the chromospheric and coronal heating.

**Key words:** MHD – Sun: atmosphere – magnetic fields

## 1. Introduction

At the photospheric level, the solar magnetic field is found to be concentrated in isolated flux tubes of different size. So called intense magnetic tubes typically have field strengths of order 1.5

kG and their diameters are about 100 km. A whole network of such intense tubes exists embedded in an almost nonmagnetic plasma (Stenflo 1978; Zwaan 1978). Sunspots on the other hand, possessing even stronger magnetic fields of a few kG and reaching diameters of several 1000 km, represent the largest members in the hierarchy of tubes.

Flux tubes on the solar surface are thought to play an important role as carrier of mechanical energy from the convection zone to the above lying atmospheric layers. Some of this energy transport takes place in the form of magnetohydrodynamic (MHD) waves which propagate along the tube. These MHD waves are excited in the convection zone as a consequence of the interaction between the flux tube and the field of turbulence. In the chromosphere and corona, the upwards transported wave energy is converted into heat by dissipative processes. Wave excitation, wave propagation, and wave energy dissipation are therefore the building blocks involved in this AC-type mechanism of chromospheric and coronal heating. The details of this wave heating picture and its relation with non-wave heating (DC-mechanisms) is presently unclear and is subject of intense research (Narain & Ulmschneider 1996).

In the present series of papers we study the dynamical response of magnetic flux tubes with various diameters to different kinds of wave perturbations. It should be noted, however, that it is only by convenience that we presently picture these tubes in a solar environment. Actually, we are interested in the basic three-dimensional behaviour of flux tubes subject to wave excitation in general and have in mind applications to stellar atmospheres and to situations in the atmospheres of accretion disks.

Due to our 3D numerical code, these investigations are not restricted to linear (small-amplitude) perturbations but allow disturbances of arbitrary amplitude. In this first paper we consider the propagation of MHD waves in thick flux tubes excited by transverse oscillations. Here, 'thick' does not necessarily mean, that the tube radius $R_0$ is large. It rather means that the quantity $\alpha = kR_0$, where $k$ denotes the characteristic wavenumber of a disturbance, is *not* assumed to be much smaller than unity as is usually the case in the so called thin flux tube approximation (see e.g. Spruit 1981ab, Cheng 1992, Ferriz-Mas

& Schüssler 1993). In our present numerical computations, $\alpha$ ranges from 0.8 to 1.8.

A proper nesting of numerical grids with successively higher resolution towards the flux tube allows to explore the structure of internal tube motions as well as to account for the possibility of the excitation of external waves due to the interaction of the tube with its surroundings. Thus, important processes like the conversion of tube wave energy via nonlinear mode coupling and by leakage to the environment can be addressed and damping rates for the flux tube waves estimated.

In a subsequent paper, numerical experiments are extended towards thin flux tubes (with small $\alpha$). In the traditional thin flux tube approximation, cross-sectional variations of all physical quantities are neglected and external pressure fluctuations are ignored. These may be critical points in the validity of the approximation which deserve special attention.

In Section 2 we discuss the basic equations and our three-dimensional numerical method. Section 3 briefly outlines the analytical investigations and Section 4 presents our results. Here the initial model, the external and internal waves, the energy leakage from the tube and the mode coupling of the tube waves are discussed. Section 5 gives our conclusions.

## 2. The method

### 2.1. Initial conditions and basic equations

We consider a vertically oriented magnetic flux tube embedded in a nonmagnetic medium. The effects of an atmospheric stratification due to gravitational forces are ignored. The neglect of stratification is rather unrealistic but considerably simplifies the problem. Inclusion of gravity will be the subject of future investigations.

The tube is assumed to be initially cylindrical with a circular cross section of radius $R_0$. The physical state of the tube and the atmosphere is characterized by constant values of the internal gas density $\rho_0$, gas pressure $p_0$, magnetic field strength $B_{z,0}$, and external density $\rho_e$. For ease of presentation, despite of a missing gravity, we picture the tube as directed along a 'vertical' z-axis and consider the perpendicular x- and y-directions as 'horizontal'. The z-coordinate is also referred to as 'height'.

Horizontal pressure balance implies

$$p_0 + \frac{B_{z,0}^2}{8\pi} = p_e \tag{1}$$

which fixes the external pressure $p_e$. Furthermore, the gas is assumed to be initially isothermal, so the internal and external density cannot be chosen independently from one another but are related by

$$\frac{\rho_e}{\rho_0} = 1 + \frac{1}{2}\gamma \frac{c_A^2}{c_S^2}, \tag{2}$$

where $c_S = (\gamma p_0/\rho_0)^{1/2}$ and $c_A = B_{z,0}/(4\pi\rho_0)^{1/2}$ are the sound and Alfvén speeds inside the tube. $\gamma = 5/3$ is the ratio of specific heats. The equilibrium state is thus written as:

$$[\rho(R), p(R), B_z(R)] = \begin{cases} [\rho_0, p_0, B_{z,0}] & R \leq R_0 \\ [\rho_e, p_e, 0] & R > R_0 \end{cases} \tag{3}$$

where $R = \sqrt{x^2 + y^2}$ is the (cylindrical) radial coordinate and $\mathbf{v} = 0$ as well as $B_x = B_y = 0$ everywhere.

The entire bottom boundary including the embedded magnetic flux tube is perturbed by a purely transverse sinusoidal oscillation in x-direction. This perturbation is expressed by a sinusoidal shaking velocity

$$v_x(x, y, z, t) = \begin{cases} \hat{v}\sin\left(\frac{2\pi t}{P}\right) & \text{near } z = 0 \\ 0 & \text{otherwise} \end{cases} \tag{4}$$

where $\hat{v}$ denotes the velocity amplitude of the perturbation and $P$ is the period of the oscillation. In the numerical realization, the layer of prescribed $v_x$ is reduced to two grid points in height at the lower z-boundary.

The use of Eq. (4) is idealized for two reasons: First, the confinement of the shaking to a narrow layer is artificial. In reality, the flux tube will be excited in a stochastic manner on a broad z-range. Second, convective motions are not purely sinusoidal. From observations (Muller 1989, Muller et al. 1994), one has a turbulence spectrum with a given distribution of amplitudes and frequencies. In more advanced simulations the mechanism of wave generation itself must be included which, however, is beyond the scope of the present paper.

The periodic disturbance in $v_x$ gives rise to MHD waves propagating along the flux tube, which may interact with the surrounding gas. The time-dependent behaviour of the excited motions is described by the following equations assuming the evolution to be adiabatic and the magnetic field to be frozen into the gas:

$$\frac{\partial \rho}{\partial t} = -\nabla \cdot (\rho\mathbf{v}), \tag{5}$$

$$\frac{\partial}{\partial t}(\rho v_x) = -\nabla \cdot (\rho v_x \mathbf{v}) - \frac{\partial p}{\partial x}$$
$$+ \frac{1}{4\pi}\left(B_z\frac{\partial B_x}{\partial z} + B_y\frac{\partial B_x}{\partial y} - B_z\frac{\partial B_z}{\partial x} - B_y\frac{\partial B_y}{\partial x}\right), \tag{6}$$

$$\frac{\partial}{\partial t}(\rho v_y) = -\nabla \cdot (\rho v_y \mathbf{v}) - \frac{\partial p}{\partial y}$$
$$+ \frac{1}{4\pi}\left(B_x\frac{\partial B_y}{\partial x} + B_z\frac{\partial B_y}{\partial z} - B_x\frac{\partial B_x}{\partial y} - B_z\frac{\partial B_z}{\partial y}\right), \tag{7}$$

$$\frac{\partial}{\partial t}(\rho v_z) = -\nabla \cdot (\rho v_z \mathbf{v}) - \frac{\partial p}{\partial z}$$
$$+ \frac{1}{4\pi}\left(B_y\frac{\partial B_z}{\partial y} + B_x\frac{\partial B_z}{\partial x} - B_y\frac{\partial B_y}{\partial z} - B_x\frac{\partial B_x}{\partial z}\right), \tag{8}$$
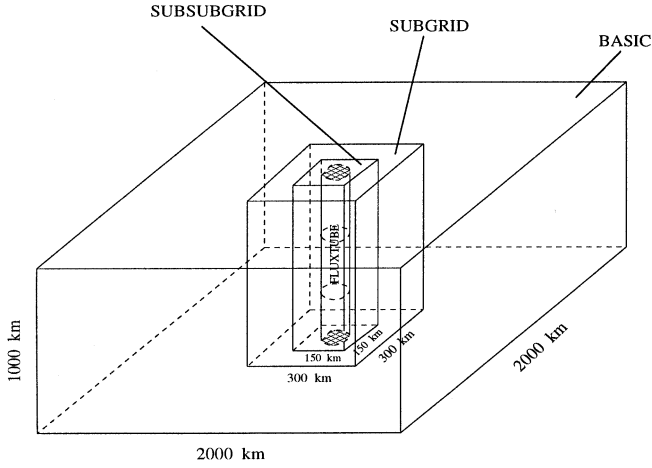
**Fig. 1.** Graphical representation of the multiple grid system used to improve the numerical resolution around the flux tube.

$$\frac{\partial e}{\partial t} = -\nabla \cdot (e\mathbf{v}) - p\nabla \cdot \mathbf{v}, \tag{9}$$

$$p = (\gamma - 1)e \; ; \qquad \gamma = 5/3, \tag{10}$$

$$\frac{\partial B_x}{\partial t} = \frac{\partial}{\partial y}(v_x B_y - v_y B_x) - \frac{\partial}{\partial z}(v_z B_x - v_x B_z), \tag{11}$$

$$\frac{\partial B_y}{\partial t} = \frac{\partial}{\partial x}(v_y B_x - v_x B_y) - \frac{\partial}{\partial z}(v_y B_z - v_z B_y), \tag{12}$$

$$\frac{\partial B_z}{\partial t} = \frac{\partial}{\partial x}(v_z B_x - v_x B_z) - \frac{\partial}{\partial y}(v_y B_z - v_z B_y). \tag{13}$$

In addition, the magnetic field **B** has to fulfill the constraint

$$\nabla \cdot \mathbf{B} = 0. \tag{14}$$

Here $\rho$, $e$, $p$, and **v** are the gas density, thermal energy density, pressure, and velocity, respectively.

### 2.2. Numerical method

The set of magnetohydrodynamic Eqs. (5)-(14) is solved with an Eulerian, time-explicit computer code using the method of finite differencing. The basic properties of the code have been described in detail in a series of papers by Stone & Norman (1992ab). The differencing scheme is second-order accurate in space using the interpolation formula of van Leer (1977) for the advection part of the code and somewhat greater than first-order accurate in time. In particular, the magnetic field is treated numerically using the so called Constrained-Transport algorithm which guarantees the divergencelessness of the magnetic field during the time evolution. Here Maxwell's equation (14) is automatically fulfilled to machine accuracy (Evans & Hawley 1988).

A multiple nested grid version of the code is applied to resolve the internal structure of tube modes. To reduce the necessary CPU time to a minimum in order to keep the problem tractable, only three nested grids are set up. A sketch of the grid system is shown in Fig. 1. The basic grid covers the domain $-1000$ km $\le x \le 1000$ km, $-1000$ km $\le y \le 1000$ km, $0 \le z \le 1000$ km adopting 100,100,50 mesh points in $x,y,z$-direction, respectively. For the numerical resolution one has $\delta = 1/\Delta = 0.05$ km$^{-1}$ with a constant grid spacing of $\Delta = 20$ km. The so called subgrid and subsubgrid is centered around the flux tube. The subgrid doubles the resolution of its spatial domain compared to the basic grid. The subsubgrid again doubles the resolution leading to an improvement of a factor of 4 relative to the basic grid. The flux tube lies entirely inside the finest grid. With a typical radius of $R_0 = 50$ km, the cross-sectional area of the tube is represented by $\approx 300$ grid points which allows for an accurate description of the internal dynamics. The physical domain, number of mesh points, and resolution of each grid is summarized in Table 1. A typical run comprised out of 700 time steps needs about 14 h CPU time on a Cray supercomputer.

Multiple nested grids have not been widely used so far to model magnetohydrodynamical flows in 3D. Thus, a brief discussion of the basics is given below. A detailed description of the method can also be found in Ziegler & Yorke (1996). Like any other grid refinement technique, the multiple nested grid scheme attempts to minimize the amount of computer time necessary to maintain a given accuracy in the numerical solution locally. The key parts of the nested grid refinement technique are the integration cycle and grid interaction processes. The integration cycle must be understood as a prescribed sequence of integrations of the individual grids necessary to evolve every grid forward in time to the same time level. Here, the subgrid is integrated twice as often as the basic grid and 4 integrations are needed for the subsubgrid in a cycle. The reason for this is that the Courant-Friedrich-Lewy criterion has to be fulfilled in explicit codes on stability grounds, which restricts the integration time step by the grid spacing. I.e. the time step allowed in the subgrid (subsubgrid) integration is just 1/2 (1/4) that of the basic grid [1].

To retain the underlying conservative character of the model equations, the individual grids cannot be regarded as independent from each other but mutually interact: Numerical fluxes of mass, thermal energy, and momentum are conserved at the coarse/fine grid interfaces forcing the differencing scheme to be conservative on the whole integration domain. In more detail, the fluxes for the coarse grid at interfaces have to be taken from the previous fine grid integration. In addition, the electromotive force in the induction equation, $\mathbf{v} \times \mathbf{B}$, has to be modified to keep the magnetic field divergence free everywhere. On the other hand, the coarse grid solution is replaced by the more accurate solution of the finer grid on its subdomain.

Apart from the time dependence in the variable $v_x$ (Eq. 4), the lower $z$-boundary at $z = 0$ is assumed to be a rigid wall. No flow is allowed through that plane. At the upper $z$-boundary, a simple outflow condition is adopted. Since the outflow boundary condition is not perfectly wave transmitting, the calculations

---

[1] Actually, the time steps of the grids are not exactly a power of 2 of the finest grid time step, because the numerical solutions slightly differ for each grid.

**Table 1.** Characteristic properties of the grid system.

| grid | domain [km] | mesh points $N_x \times N_y \times N_z$ | grid spacing $\Delta$ [km] / resolution $\delta$ [km$^{-1}$] |
|---|---|---|---|
| basic | $x \in [-1000, 1000]$ $y \in [-1000, 1000]$ $z \in [0, 1000]$ | $100 \times 100 \times 50$ | 20 / 0.05 |
| subgrid | $x \in [-300, 300]$ $y \in [-300, 300]$ $z \in [0, 1000]$ | $30 \times 30 \times 100$ | 10 / 0.1 |
| subsubgrid | $x \in [-150, 150]$ $y \in [-150, 150]$ $z \in [0, 1000]$ | $30 \times 30 \times 200$ | 5 / 0.2 |

have been stopped when the fastest wave mode was about to leave the top of the computational domain to avoid partial reflection. There is another reason for proceeding in this manner. One major aim of this work is to estimate the energy leakage rate from the tube. For this purpose any loss of wave energy due to the interaction with the boundary should be prevented. Periodic boundary conditions are used in $x$- and $y$-direction.

## 3. Analytical investigations

The nature of the wave propagation in thick magnetic tubes is very complex. This is even true for geometrically simple cylindrical tubes, immersed in a nonmagnetic, uniform atmosphere. Analytical studies of the problem are in most cases limited to linear perturbations of the tube equilibrium state by means of a Fourier analysis. There are no general results for the nonlinear regime at present.

The Fourier method is able to describe the wave propagation in the flux tube as well as in the external medium. Both media are separated by a discontinuity but may mutually interact. Because of energy conservation, the energy carried away by an external wave excited by the tube movement is taken from the tube itself, which inevitable leads to a damping of the internal motions. This damping is not a dissipative process but has to be understood analogously to the phenomenon of acoustic damping of a vibrating string. Mathematically, 'damping by acoustic radiation' can be included in a Fourier analysis by a proper matching of the internal solution to the external solution at the tube boundary. However, in this procedure damping rates can only be determined for the unrealistic case of small-amplitude perturbations. In addition, further approximations are often necessary in such analytical calculations. So far, the problem of the energy leakage has received little attention. Knowledge about the total energy loss, however, is of vital importance because it defines an upper limit for the energy fraction transferred through magnetic tubes from the convection zone to the overlying atmospheric layers.

A rather complicated dispersion relation describes the set of isolated wave modes (normal modes) which are allowed to propagate along the flux tube and defines their phase speeds. A lot of work has been devoted to the evaluation of the dispersion relation under different aspects (see e.g. Roberts & Webb (1979), Spruit (1982), Edwin & Roberts (1983)). We do not intend to review the details found in these numerous investigations. Basically, the general solution supports body waves as well as surface waves. Body waves are oscillatory waves propagating inside the flux tube. Surface waves propagate along the magnetic discontinuity having a significant energy density only near the flux tube boundary. The surface wave solution exponentially decreases perpendicular to the tube axis with a horizontal penetration length of order $k^{-1}$, where $k$ is the characteristic wavenumber of the surface wave.

Three classes of internal modes can be distinguished according to the type of perturbation. These are torsional Alfvén waves, axisymmetric magnetoacoustic waves and their non-axisymmetric counterparts. The latter two are compressive. There is only one axisymmetric mode, called sausage mode, where the wave motion is analogous to a pulsating pipe. Contrary, an infinite number of non-axisymmetric modes exist called kink modes. Kink modes are transverse waves having a polarisation perpendicular to the tube axis. The sausage mode on the other hand is a longitudinal wave i.e. the polarisation is in the direction of propagation. Generally, there is a slow and a fast compressive mode. Which of the two (or both) actually appears depends upon the physical conditions. The phase speed of the torsional waves is given by the Alfvén speed $c_A$.

The Fourier description has considerable disadvantages: As mentioned above, it supplies only normal modes. Actually, tube waves are excited by convective motions and thus in character are not free oscillations. A kind of forced oscillator mechanism is most likely to operate. What kind of modes then are excited can only be answered by a fully time-dependent calculation. Furthermore, Fourier analysis is not able to describe the effect of the so called mode conversion. Mode conversion means that due to a nonlinear coupling between different modes, energy may be transferred from one mode to another. For the chromospheric and coronal physics of particular interest is the mechanism that leads to a conversion of transversal and torsional wave energy to longitudinal wave energy because of its great importance for shock heating: longitudinal waves steepen on their upward propagation and eventually form shocks which easily dissipate the wave energy.

For the study of processes which are beyond analytical treatment such as the nonlinear mode coupling, wave damping and shock formation, one relies upon numerical models. Our present work is a natural extension of the Fourier approach dealing with the nonlinear wave propagation and should be understood as a

**Table 2.** Summary of the calculated cases.

| $\beta$ | $B_{z,0}$ [G] | $\rho_0$ [$10^{-8}$ g/cm$^3$] | $p_0$ [$10^4$ dyn/cm$^2$] | $c_A$ [km/s] | $t_{end}$ [s] |
|---|---|---|---|---|---|
| 0.1 | 1632 | 1.77 | 1.06 | 34.7 | 55.3 |
| 0.5 | 1400 | 6.50 | 3.90 | 15.7 | 62.4 |
| 1 | 1214 | 9.75 | 5.86 | 11 | 84.7 |
| 2 | 991 | 13.0 | 7.81 | 7.8 | 115.0 |
| 5 | 700 | 16.3 | 9.76 | 4.9 | 171.0 |
| 10 | 516 | 17.7 | 10.6 | 3.5 | 223.0 |

pioneer work in numerical modeling of this complex subject. Nonlinearities are automatically included by solving the full set of MHD equations (5)-(14). Because of the immense computational effort of 3D calculations, however, not all situations which may be of interest can be addressed at the present time. Our work is rather focused on a discussion of the wave structure, the efficiency of transverse-longitudinal mode conversion, and an estimation of the tube damping rate by leakage into the environment.

Unfortunately, there is no well developed theory which could serve as comparison for our calculations. From a mathematical point of view, it makes little sense to relate the numerical results to those obtained by previous Fourier analyses. However, it may be fruitful to point out the differences arising from the forced excitation and the nonlinearities in the dynamical evolution.

## 4. Results

### 4.1. The initial model

For our initial model we recall, that the effects of stratification have been ignored. The external values of the gas density and pressure are chosen to be $\rho_e = 1.95 \cdot 10^{-7}$ g/cm$^3$ and $p_e = 1.17 \cdot 10^5$ dyn/cm$^2$, respectively. These are values at the optical depth $\tau_{5000} = 1$ taken from Vernazza et al. (1981). Since the gas is assumed to be isothermal initially, the external and internal sound speeds are the same with $c_S = 10$ km/s.

The initial radius of the flux tube is $R_0 = 50$ km in all calculations. Tubes of different magnetic field strength are considered. The ratio of the internal gas pressure to the magnetic pressure, the plasma $\beta$, is defined by $\beta = p_0/(B_{z,0}^2/8\pi)$. In our work, $\beta$ is varied from 0.1 (magnetic pressure dominates) to 10 (gas pressure dominates). From the condition of pressure balance (Eq. (1)) and from Eq. (2), the internal values $p_0$ and $\rho_0$ are derived. A summary of all calculated models is given in Table 2 including the initial physical state of the tubes ($\beta$, $\rho_0$, $p_0$), the Alfvén speeds $c_A$, and the stopping times of the calculations $t_{end}$.

It remains to specify the characteristic properties of the perturbation. For all cases summarized above, we take a velocity amplitude of $\hat{v} = 2$ km/s and a wave period of $P = 50$ s. $\hat{v}$ defines the energy flux introduced into the tube. The energy fluxes of the order $10^8$ to $10^9$ erg cm$^{-2}$ s$^{-1}$ (depending upon the physical state of the tube) are comparable to those which have been computed for transverse tube waves generated by the turbulent

motions in the solar convection zone (Huang et al. 1995, note that their values should be corrected upwards by roughly a factor of 3 as discussed by Ulmschneider & Musielak 1997).

### 4.2. The external waves

Figs. 2 and 3 show snapshots of the excited motions for a tube with plasma $\beta = 1$. The full computational domain is shown (recall, that there is much more detailed information available for the inner parts of the physical domain than Figs. 2 and 3 indicate, this internal structure is discussed below). The snapshots show the velocity field at time $t_{end} = 84.7$ s (see Table 2). Fig. 2 refers to a horizontal plane at height $z = 160$ km, while Fig. 3 shows a vertical plane through the tube axis in swaying direction given by $y = 0$. At least two different types of waves can be distinguished: a predominantly transversal internal body wave, which propagates upwards along the tube and an external wave (indicated by dots) which propagates into the surrounding medium. For the sake of completeness, we remark that there is a third kind of wave present but not emphasized in the figures, namely a surface wave which is confined to the flux tube boundary. A single contour line defined by either $B(x, y) = B_{z,0}/2$ (Fig. 2) or $B(x, z) = B_{z,0}/2$ (Fig. 3) is overlaid in both figures to visualize the tube boundary. Similar definitions for tube boundaries will be used later in the other figures without mentioning it explicitly. We now discuss the external wave in more detail and later in Section 4.4 turn to the internal dynamics of the flux tube.

Since the surrounding medium is assumed to be nonmagnetic, the external wave is a pure sound wave where the relevant phase speed is given by the sound speed $c_S$. The external 'acoustic radiation field' shows a degree of anisotropy in space (cf. Fig. 2) which is due to the preferred direction of the velocity perturbation. The appearance of the external acoustic field may be thought of as a superposition of isotropically propagating elementary sound waves excited by each surface element of the flux tube. Note, that external to the tube there is no direct excitation by the perturbation at the lower $z$-boundary. The induced pressure fluctuations are seen to be largest where the gas is compressed most strongly by the tube boundary. This is expected to be the case in the direction of the perturbation, leading to the asymmetry seen in Fig. 2.

From a linear Fourier analysis, the criterion for the existence of an external oscillatory mode has been found to be $c_{ph} > c_S$ i.e. the phase speed $c_{ph}$ of the internal mode exceeds the (external) sound speed $c_S$ (Spruit 1982). Actually, the phase speeds of our tube waves are found to be less than $c_S$ (cf. Table 3). Following Spruit's argument, the external wave ought to be evanescent in contradiction to the results of our nonlinear simulation. Clearly, his analysis is only valid for small-amplitude perturbations far away from any switch-on phase. In addition, the derivation of the above criterion has been carried out for the marginal limit of vanishing damping rate of the tube (i.e. the fraction of energy lost to the surroundings tends to zero) which correctly describes only the idealized situation of an infinitesimal thin flux tube in his analysis. If a significant transfer of tube
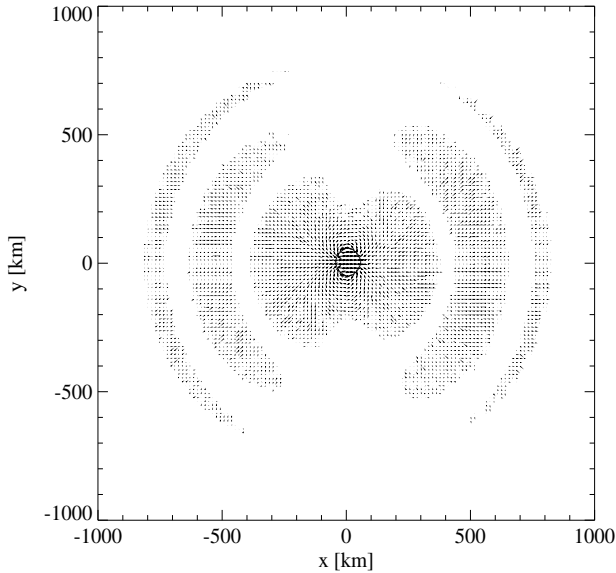
**Fig. 2.** Snapshot of the horizontal velocity field in the plane $z = 160$ km ($v_{max} = 0.55$ km/s). The flux tube boundary is indicated (drawn).
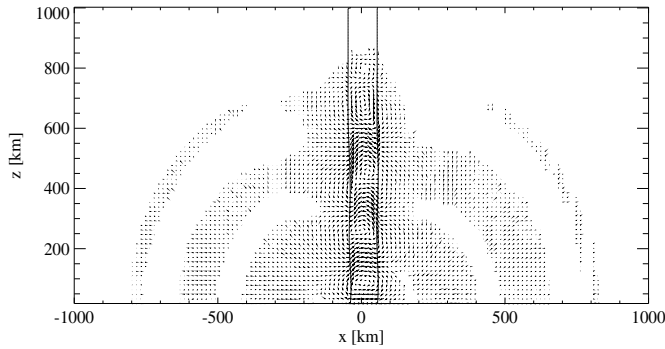


**Fig. 3.** Snapshot of the vertical velocity field in the plane $y = 0$ ($v_{max} = 0.80$ km/s). The flux tube boundary is indicated (drawn).

energy to the surroundings is expected, however, the criterion may break down. This is because in general, the damping rate itself enters the dispersion relation through the imaginary part of the (tube) wave frequency $\omega$ which was not considered by Spruit. As will be shown later, damping rates up to 0.43 are obtained (depending on $\beta$) which means that almost half of the total wave energy is used to feed the external mode.

Fig. 4 shows the variation of $v_x$, $B_x$, $\rho$, and $p$ in a 1D cut along the $x$-axis in the vertical plane going through the tube axis, $y = 0$, at height $z = 160$ km. Here the external velocity ($v_x \approx 0.02$ km/s), which is typical for the external velocity amplitude $\hat{v}_{sound}$, is seen to be less than the internal velocity amplitude ($v_x \approx 0.4$ km/s) by a factor of about 20. For the relative fluctuations of the external gas density and pressure, we find within an order of magnitude $\delta\rho/\rho = \delta p/p \approx 10^{-3}$. These values have to be compared with the fluctuations occurring inside the tube, namely $\delta\rho/\rho = \delta p/p \approx 10^{-2}$. Although the external wave energy density is shown to be small, the total

wave energy stored in the external field is not. This is because the outside medium represents a much larger space than the tube itself. As already mentioned, the energy carried away by the external wave originates from the tube motions. To what extent internal waves are influenced by this damping process thus depends on the amount of energy leakage discussed in a subsequent section below.

### Dependence on $\beta$

Our numerical results show that there always exists a propagating external wave for the $\beta$-range (0.1 to 10) considered here. The main difference is in the amplitude of the fluctuations. We found it to decrease with increasing $\beta$. This may be explained in terms of the 'relative compressibility' of the external medium. A quantity appropriate to describe this term is given by the ratio of the Alfvén speed to the (external) sound speed, $c_A/c_S$. It expresses the fact that the external gas (characterized by $c_S$) is the more compressed the more resistance the swaying tube puts up. A high resistance corresponds to a high magnetic field strength inside the tube (low $\beta$ or high $c_A$) which means that the tube is more 'rigid' pushing the outer gas harder. From this point of view, the external gas is expected to be less perturbed for increasing $\beta$ which results in a lower $\hat{v}_{sound}$.

### 4.3. Damping rates by leakage

In order to investigate the leakage of energy from the flux tube we have to list carefully the relevant energies inside and outside the tube. The total *wave* energy (internal plus external) is given by the sum

$$E_{tot}(t) = E_k(t) + E_m(t) + E_{th}(t), \tag{15}$$

where $E_k = E_{k,x} + E_{k,y} + E_{k,z}$, $E_m$, and $E_{th}$ are the time-dependent contributions of the total kinetic wave energy, total magnetic wave energy, and thermal wave energy, respectively. Let us denote the perturbed quantities in the usual manner by a prime: $\rho' = \rho - \rho^{(0)}$, $e' = e - e^{(0)}$, $\mathbf{v}' = \mathbf{v}$, $B_x' = B_x$, $B_y' = B_y$, and $B_z' = B_z - B_z^{(0)}$, where the superscript (0) refers to unperturbed values of the equilibrium state. Expressions for the various forms of energy valid for arbitrary perturbation amplitudes are:

$$E_{k,x}(t) = \frac{1}{2}\int \rho v_x'^2 dV, \tag{16}$$

$$E_{k,y}(t) = \frac{1}{2}\int \rho v_y'^2 dV, \tag{17}$$

$$E_{k,z}(t) = \frac{1}{2}\int \rho v_z'^2 dV, \tag{18}$$

$$E_m(t) = \frac{1}{8\pi}\int \left[ B_x'^2 + B_y'^2 + B_z^2 - (B_z^{(0)})^2 \right] dV, \tag{19}$$
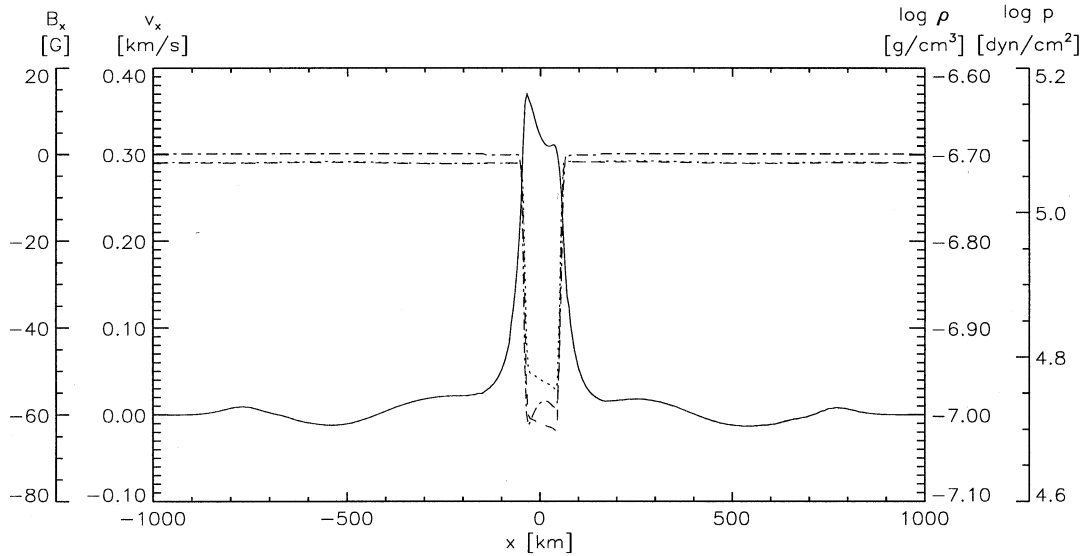
$$E_{th}(t) = \int e' dV. \tag{20}$$

**Fig. 4.** One-dimensional cut in swaying direction ($y = 0$) through the tube axis at height ($z = 160$ km) showing the variation of $\rho$ (dashed line), $p$ (dotted line), $v_x$ (solid line), and $B_x$ (dash-dotted line) with horizontal position $x$.

For later use, it is helpful to define time-averaged quantities according to

$$\langle E \rangle(t) = \frac{1}{t} \int_0^t E(t')dt', \qquad (21)$$

where $E$ stands for any of the wave energies above. Eqs. (16) to (20) can be written for the internal region of the tube or for the external medium alone. In the following, the internal energies are denoted by a superscript 'i' and the external quantities by 'e'. We now define the damping rate by leakage $D(t)$ from the tube as the ratio of the mean values of the total external wave energy to the sum of both the total external and internal wave energies. It is a quantitative measure for the amount of energy which leaks out of the tube. This ratio can be written as

$$D(t) = \frac{\langle E_{tot}^e \rangle}{\langle E_{tot}^e \rangle + \langle E_{tot}^i \rangle}. \qquad (22)$$

This definition also includes that part of the external wave energy which may be reabsorbed by the tube (see eg. Goossens & Hollweg 1993, Stenuit et al. 1993). To simplify the notation, the dependence of the mean quantities on time has been dropped. For $t \gg P$ i.e. the time is much larger than the period of the oscillation, it is intuitively expected that $D(t)$ tends to a constant value $D$. This is because averaged over many periods, the switch-on phase of wave excitation has decayed and a steady state develops with $D$ being dependent only on the physical parameters ($\beta$). However, the condition $t \gg P$ cannot be reached in our present numerical setup of the problem and $t$ is limited by $t_{end}$ which amounts to at most a few periods (cf. Table 2).

We have numerically calculated $D(t)$ using the above formulae. The time evolution is illustrated in Fig. 5 with $\beta$ as parameter. Note that after an initial violent phase, the damping rate tends towards a steady state most prominent for the high $\beta$ tubes
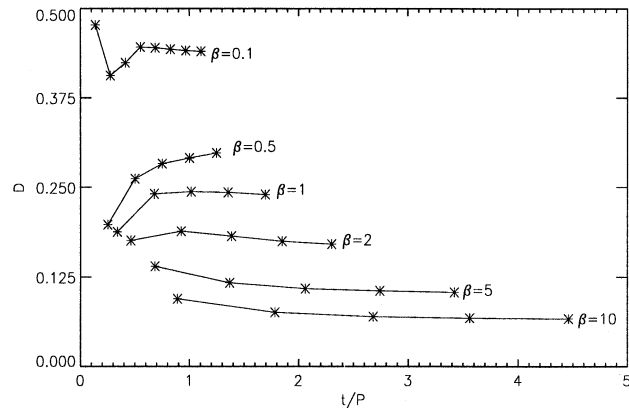


**Fig. 5.** Damping rate by leakage $D$ as function of the dimensionless time $t/P$ for different $\beta$ (The actual calculated values are indicated by '*' connected by lines).

although the condition $t \gg P$ is not yet satisfied. If the value at $t_{end}$ is taken, then D is a monotonically decreasing function of $\beta$. The magnitude of the energy loss varies from $D \approx 0.4$ for the $\beta = 0.1$ tube (magnetic pressure dominates) to a value of $D \approx 0.07$ for the gas pressure dominated $\beta = 10$ tube. For the low $\beta$ tubes this is a significant portion of the generated energy and, therefore, for these cases energy leakage cannot be ignored in studies of magnetic tube waves. As already indicated, the reason for the decline in the leakage is the decrease in the amplitude of the external fluctuations (resulting in a lower total external wave energy) because the relative compressibility of the surrounding gas drops.

Xiao (1988) and more recently Huang (1995, 1996) have explored the (non)linear wave propagation in magnetic slabs. In their 2-dimensional adiabatic simulations, they have estimated
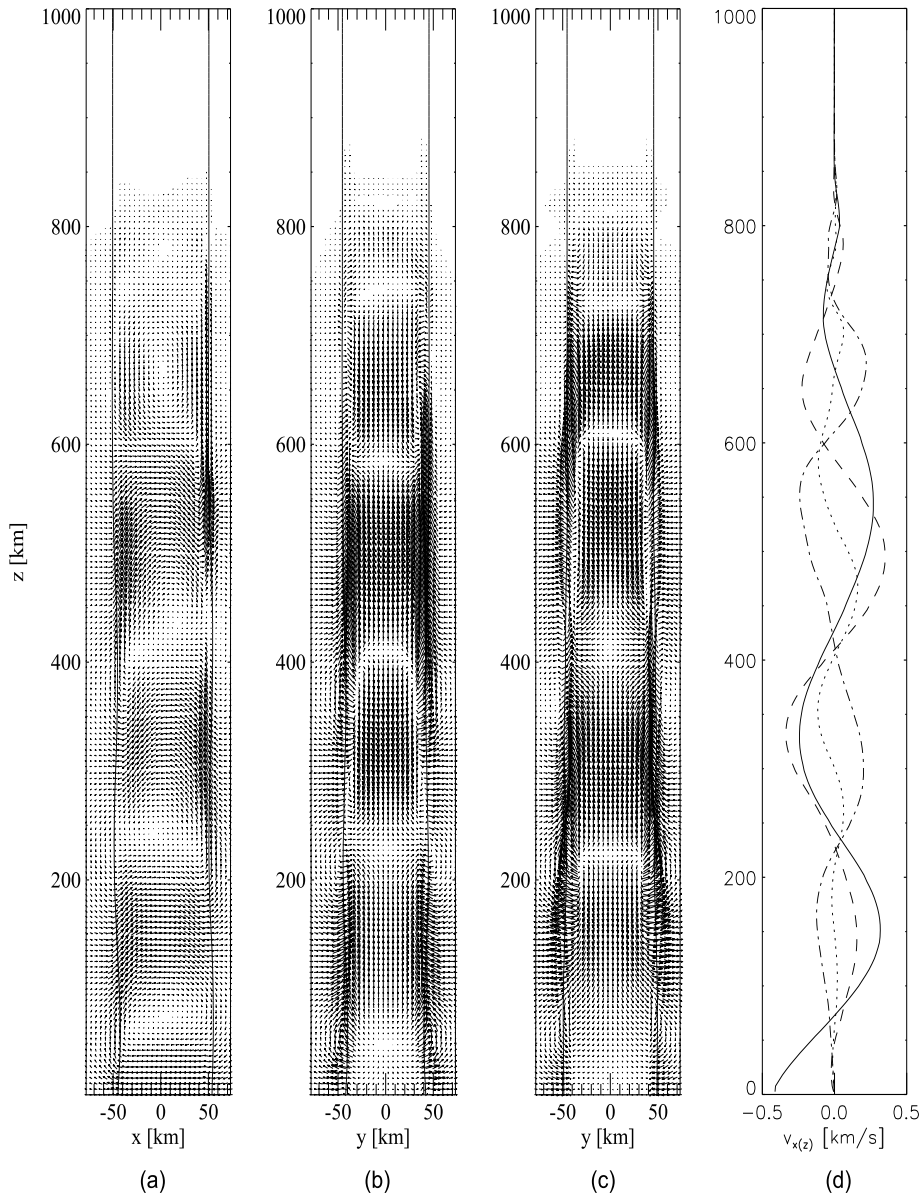
**Fig. 6. a** v-field in the plane $y = 0$ ($v_{max} = 1.32$ km/s), **b** v-field in the plane $x = -22.7$ km ($v_{max} = 0.48$ km/s), **c** v-field in the plane $x = 22.7$ km ($v_{max} = 0.33$ km/s), and **d** One-dimensional cuts through the tube illustrating the $z$-variation of $v_x$ (solid line: cut through $(x, y) = (0, 0)$) and $v_z$ (dashed line: cut through $(x, y) = (-22.7, 0)$ km, dash-dotted line: cut through $(x, y) = (22.7, 0)$ km, dotted line: cut through $(x, y) = (0, 0)$ - in this last case, $v_z$ is multiplied by a factor 2).

the damping rate by leakage for transverse perturbations assuming an environment with similar thermal properties than we applied. Huang found rates which are higher than ours by a factor of $\approx 2$ for the $\beta = 1$ tube and $\approx 5$ for the $\beta = 10$ tube. We explain the discrepancy between our and their results as due to the geometry of the magnetic structure. The impact of a slab on the surroundings is much larger than that of a cylindrical tube, because the effective area of the tube interacting with the environment, is smaller. Therefore, slab models are not very good means to estimate the energy loss of waves propagating along tube-like magnetic structures. In doing so, one significantly overestimates the energy loss.

### 4.4. The internal waves

We now consider the motions inside the tube and near its surface in more detail. As in the discussion of the external wave, we start with the case $\beta = 1$. In Figs. 6, the velocity structure taken

from the subsubgrid is shown in form of 2D vector fields in different planes parallel to the tube axis. For ease of presentation we distinguish in the swaying $x$-direction between the forward direction ($+x$) and backward direction ($-x$). Fig. 6a is a cut through the tube axis in swaying direction. Figs. 6b and 6c are cuts parallel to the tube axis and perpendicular to the swaying direction, 22.7 km backwards and forwards of the tube axis, respectively. Finally, Fig. 6d shows 1D cuts in vertical direction illustrating the variation of the components $v_x$ and $v_z$ with height $z$ taken at fixed points of the cross section.

Although the perturbation is purely transverse, various types of waves are excited: a transverse body wave, longitudinal body waves, and a surface wave. Most likely, all types of waves seen belong to the family of slow waves. Their faster counterparts are not observed and may be prohibited because of the assumed isothermal environment or perhaps because they are too weak to be visible. The absence of fast modes agrees with Fourier

results obtained for thin flux tubes (Spruit 1982). There, it was found that fast waves only occur if the tube plasma is cooler than the surrounding gas. But this is not the case here.

*Transverse body wave*

The transverse body wave is clearly seen in Fig. 6a as well as in Figs. 8. Owing to the purely transverse shaking in x-direction the tube at heights $z = 160, 500$ km (Figs. 6a, 8b) shows flows in $+x$ and at heights $z = 0, 340$ km (Figs. 6a, 8d) flows in $-x$ across the entire tube cross-section. Due to these flows, Fig. 6a shows maximum excursions of the tube boundaries in the x-direction at the heights of $z \approx 60, 220, 400$ km. This transverse body wave can be easily understood as a direct result of the applied swaying perturbation. Its frequency $\omega$ is related to the oscillation period $P$. However, in analogy to a damped forced oscillator, $\omega$ is not precisely given by the relation $\omega = 2\pi/P$, but is modified due to the damping rate of the tube. The phase speed $c_{ph}$ of the transverse body wave cannot be given in terms of a single number because there is no unique phase speed.

From the numerical data, a value of $c_{ph} \simeq 7.6$ km/s (7.0 km/s, 6.8 km/s) is measured from the wave peaks (nodes, troughs). For comparison, linear kink-type body modes propagate roughly with a phase speed $c_T$ valid for long-wavelength disturbances i.e. $\alpha \ll 1$ (Edwin & Roberts 1983), where $c_T$ is the well-known tube speed given by

$$c_T = \frac{c_S c_A}{\sqrt{c_S^2 + c_A^2}}. \tag{23}$$

More generally, tube waves are dispersive i.e. their phase speeds depend on the wavelength. For $\alpha$ not too large, dispersive effects are small (cf. Fig. 3 in Edwin & Roberts 1983). Thus, to a first approximation one has $c_{ph,linear} \simeq c_T$ for the $\alpha$-regime considered here. For the $\beta = 1$ tube, a value of $c_T = 7.4$ km/s is derived. This has to be compared with the measured values $c_{ph}$ given above. We attribute the discrepancy between $c_{ph}$ and $c_T$ to the nonlinear character of the propagation, to the switch-on effects and to uncertainties regarding the influence of the forced excitation. For the latter, note that at time $t_{end}$ the transverse wave has just propagated for two wavelengths.

*Longitudinal waves*

As we did not excite it by direct perturbation, the longitudinal wave seen in Figs. 6b and 6c is generated as a consequence of the transverse motion. This wave, indicated by longitudinal velocities $v_z$, is clearly seen to be a body wave. It results from a coupling between the transversal and longitudinal wave modes. Transverse-longitudinal mode coupling is a universal property of wave propagation in flux tubes. That is, a transverse wave is always accompanied by longitudinal motions i.e. part of the transverse wave energy has been used to feed the longitudinal mode.

The generation of a longitudinal wave can easily be understood in the thin flux tube limit: The restoring force for horizontal displacements is the magnetic tension force which always
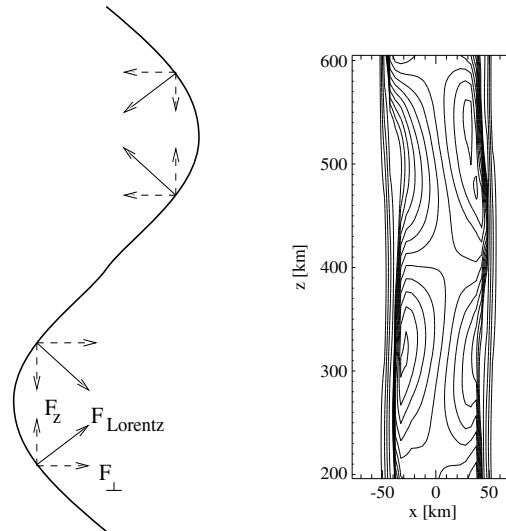


**Fig. 7.** Left: Occurrence of a longitudinal mode in thin flux tubes due to a vertical component of the magnetic tension force. Right: pressure contour lines in the plane $y = 0$. Contour lines are chosen non-equidistant to indicate pressure variations inside the flux tube which otherwise were not visible due to the strong gradient at the surface.

acts in the direction to the local center of curvature of the tube (Fig. 7, left panel). This force possesses a vertical component which gives rise to rarefactions and compressions along the tube. From the figure it is clear that a sausage-type fundamental longitudinal wave mode is excited with a dominant frequency twice as large as the frequency $\omega$ of the prevailing transverse wave. The doubling of the frequency is due to the sign reversal of the vertical force component. It changes its sign twice while the horizontal component does only once in a transverse wavelength (Ulmschneider et al. 1991).

The prominent longitudinal wave observed in Figs. 6b and 6c, however, is not of the fundamental sausage-type but shows a non-axisymmetric velocity pattern. Note e.g. that at a height $z = 500$ km the backward y-slab (Fig. 6b) shows everywhere positive $v_z$ velocities, and the forward y-slab (Fig. 6c) negative $v_z$ velocities at the same height, while at the tube axis (Fig. 6a) one has longitudinal velocities close to zero. Clearly, this is not the fundamental longitudinal body wave mode which would be expected to show similar velocities $v_z$ across a given cross-section.

The non-axisymmetric structure cannot be explained by the action of magnetic tension forces, responsible for the sausage-type wave in the case of a thin flux tube. The reason for the departure from axisymmetry are variations in the total (gas plus magnetic) pressure $p_{total}$ across the tube which in the thin flux tube approximation are ignored and which become important and play a major role in our dynamical computations. More precisely, a gradient in the direction of the perturbation develops while $\partial p_{total}/\partial y$ approximately vanishes. Moreover, the gradient of the gas pressure is found to dominate over the gradient of the magnetic pressure which has the opposite sign.
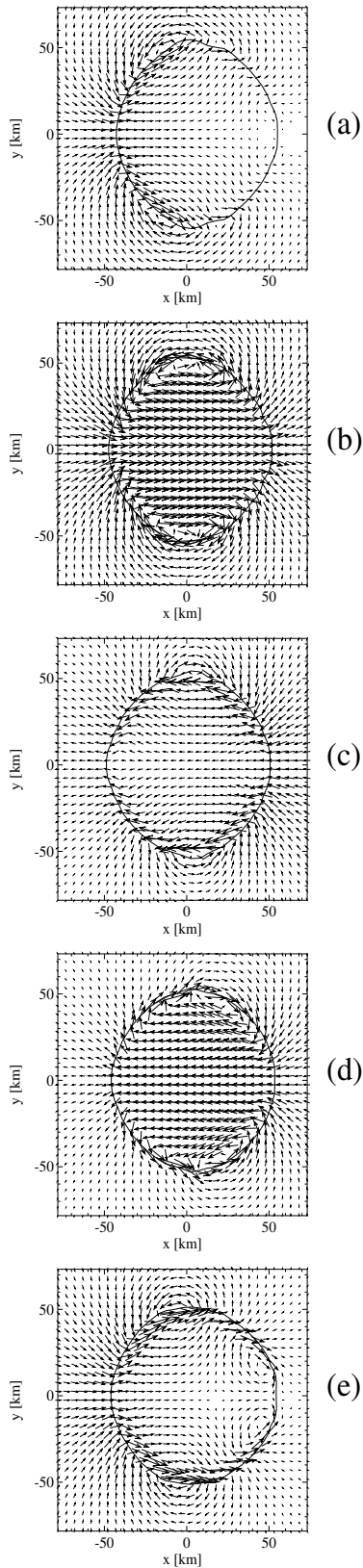
**Fig. 8a-e.** Velocity structure in slices perpendicular to the tube axis. The planes $z = 75$ km (**a**), $z = 163$ km (**b**), $z = 250$ km (**c**), $z = 338$ km (**d**), and $z = 425$ km (**e**) are shown, respectively. The maximum velocity is given by 0.50 km/s.

We believe that the reason for this behaviour lies in the inertia of the tube plasma resisting transverse accelerations. This explanation is supported by the sign of the induced gradient. It is found to be anticorrelated with the sign of $\partial v_x / \partial t$. If $\partial v_x / \partial t > 0$, a gradient $\partial p_{total} / \partial x < 0$ exists while $\partial v_x / \partial t < 0$ involves $\partial p_{total} / \partial x > 0$. Thus the variations in $p_{total}$ over the tube cross-section are generated by the transverse motion.

A transverse gradient of the gas- or magnetic pressure, however, involves a vertical gradient of the same quantity. This can be seen from Fig. 7 (right panel) which shows the gas pressure distribution at $t_{end}$ in the vertical plane given by $y = 0$. From the shape of the contour lines inside, it is obvious that there are pressure gradients both in $x$- and $z$-directions. This means that a compressional restoring force operates in addition to the magnetic tension force which influences motions in a drastic way: Longitudinal waves develop on both sides of the tube separated by the plane $x = 0$. However, the neighboring waves suffer a phase difference of $\approx \pi$ (see Fig. 6d) which manifests itself in a non-axisymmetric velocity pattern.

Together, the vertical component of the magnetic tension force and the induced vertical gradient of the total pressure are the basic driving mechanisms for the internal longitudinal mode. Which of the two processes actually predominate, depends upon their relative strengths and their variation with position across the tube. There is a fundamental difference between both mechanisms worth to emphasize regarding the frequency of the excited wave. Mode-coupling due to the magnetic tension force leads to a frequency $2\omega$ while the inertial pile-up mechanism discussed above to a dominant frequency $\omega$. We find that the restoring force due to the inertial compression is by far more powerful, except near the plane $x \approx 0$. A special situation arises there: The vertical pressure gradients induced by transverse pile-up are seen to be negligible and longitudinal wave excitation is exclusively caused by the vertical component of the magnetic tension force. The expected $2\omega$-type longitudinal sausage wave is indeed observed in the numerical computations and can be seen from Fig. 6d which shows the velocity $v_z$ (dotted) at the position $(x, y) = (0, 0)$ close to the tube axis. Note that compared to the transverse velocity $v_x$ (drawn), $v_z$ indicates a doubling of the frequency.

*Surface wave*

The surface wave can be best seen from Figs. 6b and 6c where the velocity vectors are strongly concentrated at the tube boundaries. It is also seen in all of the Figs. 8, where it shows itself as a distinct motion close to the tube boundary. Note that despite of the shaking purely in $x$-direction, the velocity has $y$-components which change in direction along the $z$-axis. Moreover, it is seen in Fig. 6a, as well as by comparing Figs. 6b and 6c, that the surface wave has a phase delay between the forward and backward sides of the tube. This is also seen in the cross-section (Figs. 8a, 8e). Fig. 8a taken at height $z = 75$ km, shows an instant of time, where the tube after considerably swaying in forward direction at the forward part of the tube has come to rest with a maximum excursion, while the backward part of the tube be-
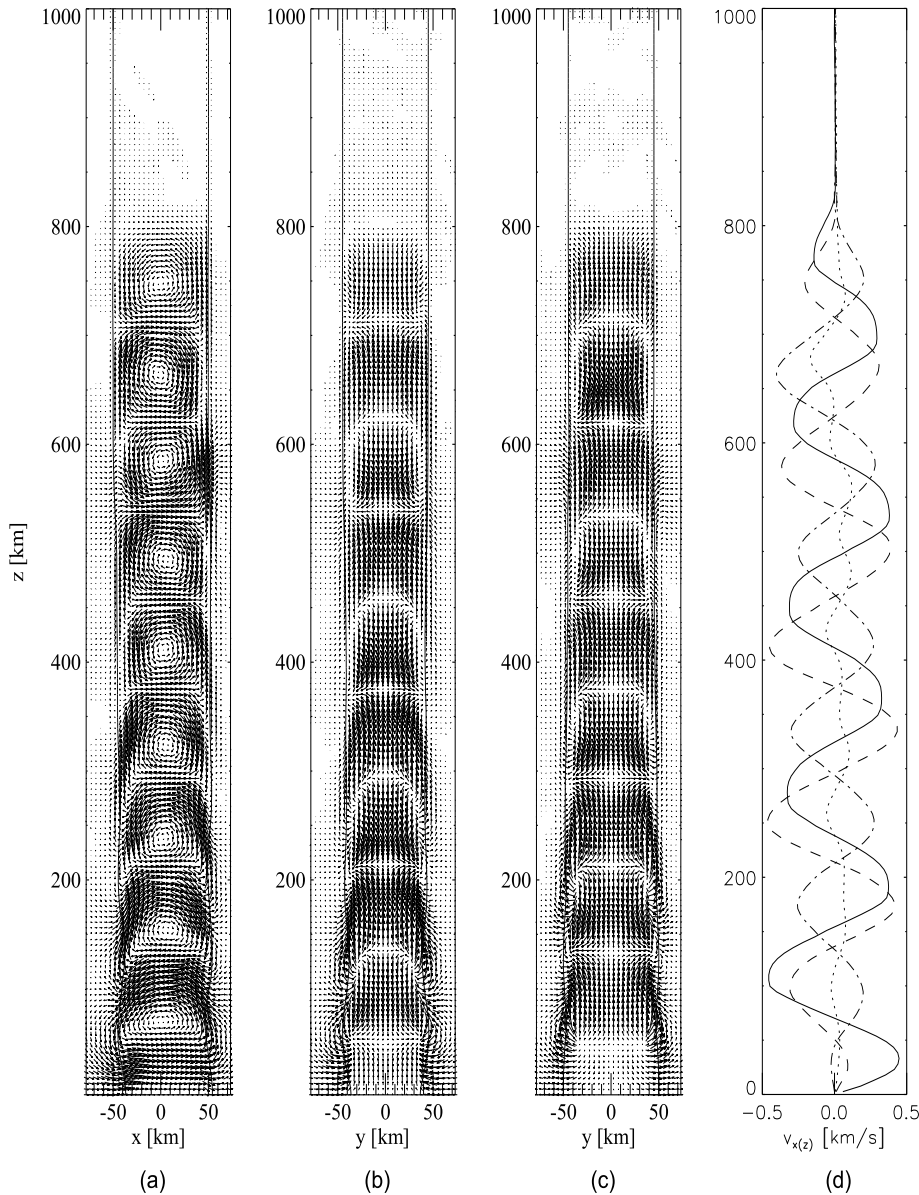
**Fig. 9a-d.** Similar to Figs. 6 for $\beta = 10$, however, **a** $v_{max} = 0.72$ km/s, **b** $v_{max} = 0.48$ km/s, and **c** $v_{max} = 0.40$ km/s.

ing delayed, still moves in forward direction. Fig. 8e shows the same situation at height $z = 425$ km. In Fig. 6a it is seen that at the backward side the maximum $+x$ excursion of the tube boundary is still at $z = 60$ km, and thus will arrive at the height displayed in Fig. 8a at a later time. The phase delays thus lead to different heights of the maximum tube excursions at the forward and backward sides of the tube.

From these discussions and particularly from Figs. 8 it is clear that the surface wave is generated by the interaction of the internal body waves with the tube surface and by the backreaction of the surrounding compressible medium onto the tube. The penetration distance of the surface wave at the tube boundary can be estimated from Figs. 6b, 6c and 8. We find roughly a value of 15 km which is much less than the tube radius. Outside this distance, the surface wave energy density is negligible.

Note that the originally cylindrical shape of the tube cross section changes into a more oval shape with the short diameter in swaying direction. Note also that the horizontal displacement of the tube boundary trails $v_x$ by $\approx \pi/2$ in phase, and that $v_x = 0$ appears where the bending of field lines is strongest (Fig. 6a). This has already been found by Ulmschneider et al. (1991) for thin flux tubes.

### 4.5. Tubes of different magnetic field strength

Up to now we have considered the internal behaviour of a tube with $\beta = 1$. In this section we discuss how this behaviour changes when the magnetic field strength varies. The way by which the variation of the magnetic field strength influences the external medium when a transverse wave is excited, has already been discussed in Sections 4.2 and 4.3, so we concentrate here on the internal structure of the tube. Figs. 9 and 10, similar
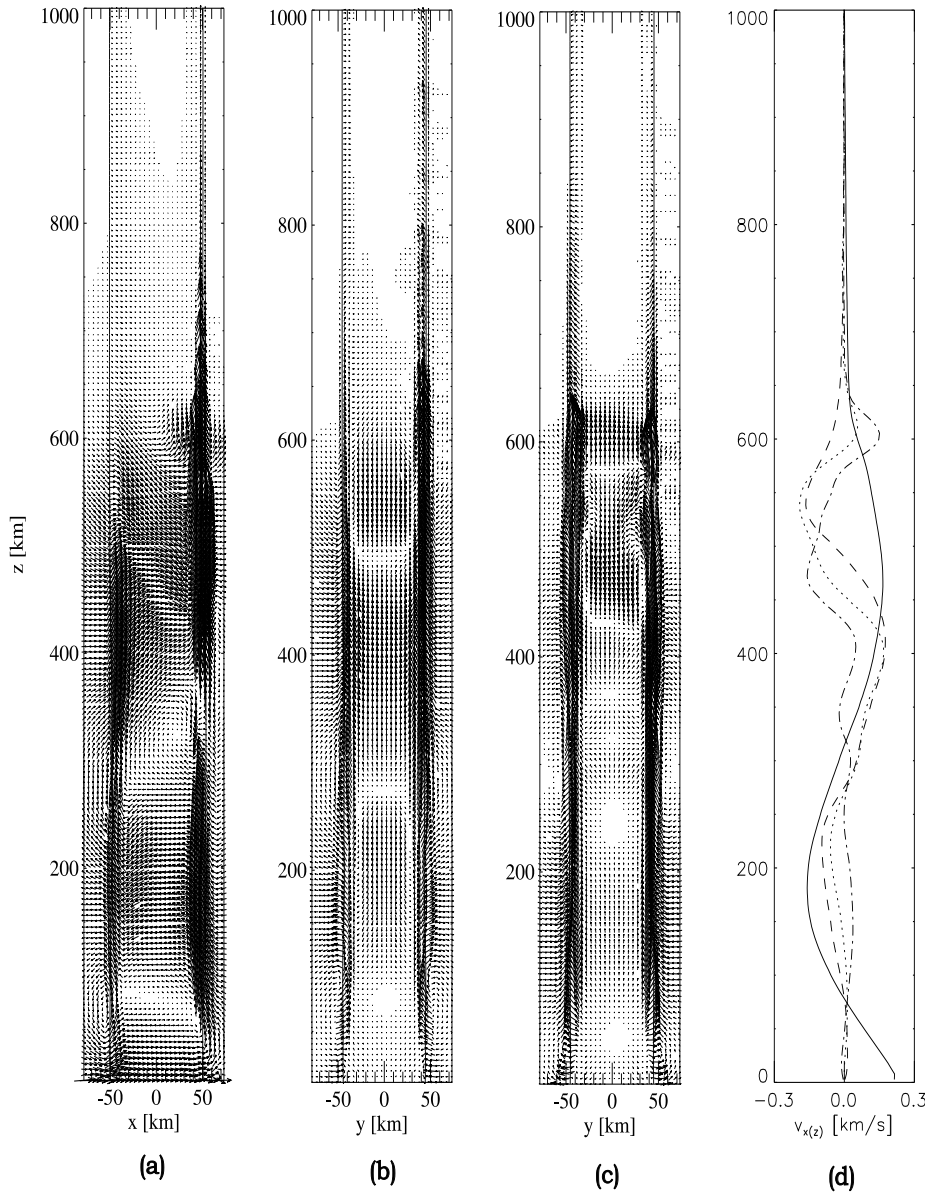
**Fig. 10a-d.** Similar to Figs. 6 for $\beta = 0.1$, however, **a** $v_{max} = 0.60$ km/s (Note that even larger velocities (up to 3 km/s) occur at the surface in a height $z \approx 500$ km which were cutted to give a better description of the internal velocity pattern), **b** $v_{max} = 0.90$ km/s, and **c** $v_{max} = 0.65$ km/s.

to Figs. 6, show wave calculations for the cases $\beta = 10$, and $\beta = 0.1$, respectively. In addition, in Figs. 11 we display tube cross sections at various heights for these calculations. These figures show major differences in the internal structure.

a. In the $\beta = 10$ tube magnetic forces are weak and thus the phase speed is reduced compared to that of the $\beta = 1$ tube. Since the wave frequency is prescribed as a boundary condition, one obtains a shorter wavelength (Figs. 9a, 9d). Similarly for the $\beta = 0.1$ tube a longer wavelength is found (see Figs. 10a, 10d). Here a stronger magnetic field leads to a higher phase speed, resulting in a longer wavelength. Table 3 summarizes the measured phase speeds together with the computed tube speed $c_T$. It is seen that the phase speed is essentially equal to $c_T$ for high $\beta$. This shows that the phenomena in the tube are dominated by $c_T$.

b. Similarly to the $\beta = 1$ case, the $\beta = 10$ tube shows even more pronounced non-axisymmetric longitudinal flows which in Fig. 9a take on almost the appearance of a sequence of cylindrical rolls successively rotating clock- and counterclockwise around a $y$-axis. This cylindrical roll-like appearance is also seen in the cross sections, where the originally circular tube cross section has been modified into an oval shape. These motions imply that with increasing $\beta$ the magnetic resistance to circulatory flows decreases. Note that despite of weaker magnetic field in this tube there is a distinctly different surface wave behaviour of the region near the tube boundary. In this boundary region the flow inside the tube is very similar to that outside the tube.

c. While going from the $\beta = 1$ to the $\beta = 10$ tube increases the roll-like appearance, the opposite is true when going to $\beta = 0.1$. Here, the strength of the non-axisymmetric longitudinal body wave appears to be much reduced. These flows in Figs. 10b
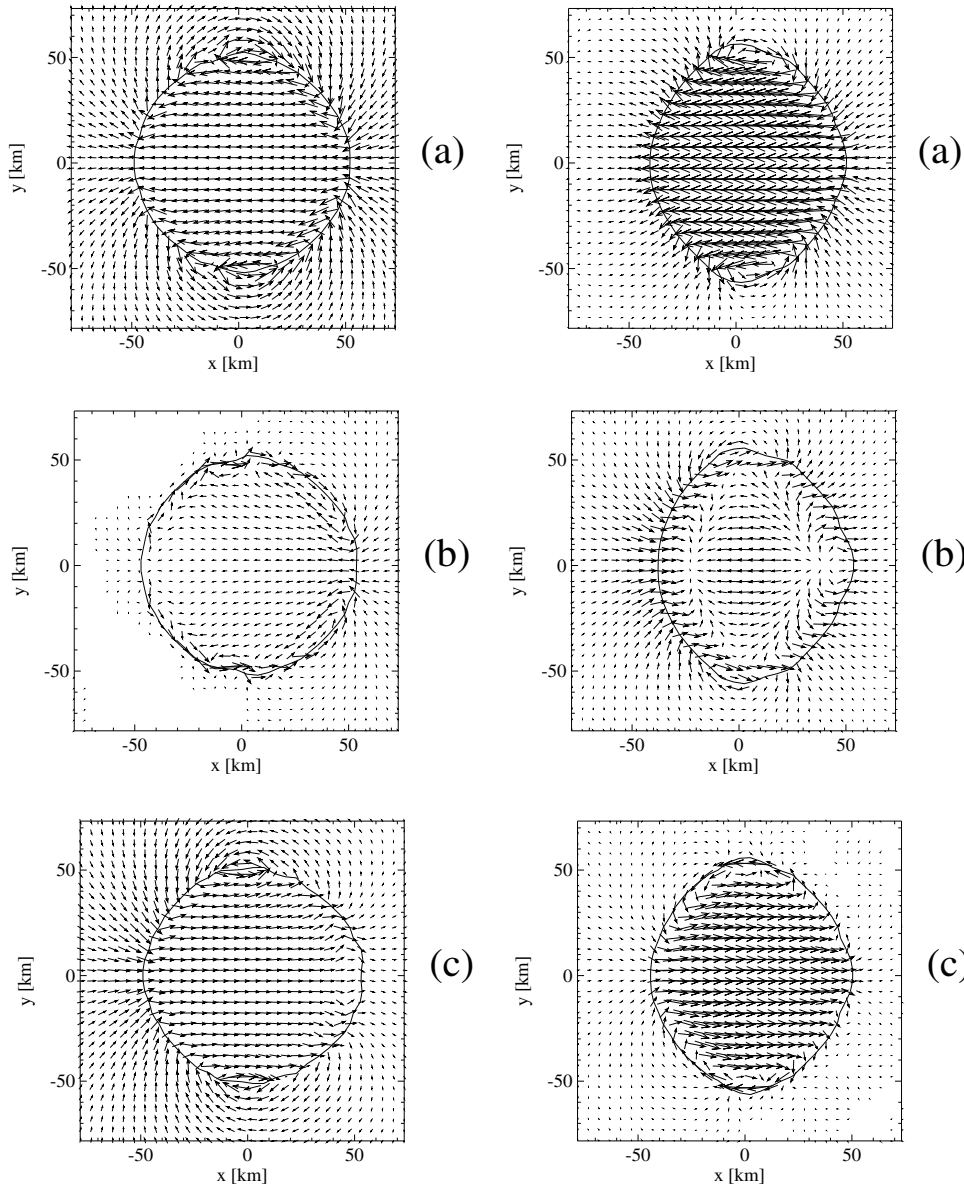
**Fig. 11a-c.** Similar to Figs. 8 for the cases $\beta = 10$ (left pannel) and $\beta = 0.1$ (right pannel). Left, the planes $z = 100$ km (**a**), $z = 140$ km (**b**), and $z = 180$ km (**c**) are shown, respectively ($v_{max} = 0.48$ km/s). Right, the planes $z = 150$ km (**a**), $z = 275$ km (**b**), and $z = 400$ km (**c**) are shown, respectively ($v_{max} = 0.40$ km/s).

and 10c are noticeably smaller particularly at lower height. On the other hand, the strength of the surface wave appears to be considerably increased compared to the high $\beta$ cases. This can be explained by the fact that the tube becomes more rigid leading to a harder interaction with the external gas. In addition, the parts of the wave above $z > 380$ km indicate a strong switch-on effect.

d. A comparison of the cross sections of the cases $\beta = 10$ and $\beta = 0.1$ shows that the low $\beta$ tube largely retains its original circular shape. This is due to the fact that the compressibility of the tube decreases, which makes low $\beta$ tubes much more rigid. Note that this increase in rigidity is also seen in the decreased amplitude of the excursions of the tube boundary in x-direction in Fig. 10a as compared to Fig 9a.

e. The complexity of internal motions increases as the dominance of the magnetic field grows. The surface phenomena become relatively more important at the same time. Figs. 9a and

9d show that clear wave patterns are found for the $\beta = 10$ tube while for the $\beta = 0.1$ tube the longitudinal wave, for instance, does not have a simple periodic structure. But here very likely, the switch-on effect is still at work.

f. A strong surface feature is observed for the $\beta = 0.1$ tube at height $\approx 500$ km (see Fig. 10a, but also Figs. 10b, 10c). Here a strong longitudinal pulse is concentrated near the tube boundary which propagates upwards with velocities of up to 3 km/s. We believe that this pulse is the result of the initial violent switch-on phase. It is expected that for decreasing $\beta$ due to the decreasing ratio $t_{end}/P$ the switch-on effects become more pronounced but also, because the rigidity of the tube is increased.

## 4.6. The efficiency of mode conversion

We now want to estimate the amount of mode-conversion from the transverse to the longitudinal mode. This mode conversion

**Table 3.** Basic properties of the transverse body wave: phase speeds (measured), wavelength (calculated using the phase speed measured for the node and the period $P$), thinness parameter $\alpha$, and tube speed $c_T$. The case $\beta = 0.1$ is missing because $c_{ph}$ could not measured. The external sound speed is $c_S = 10$ km/s.

| $\beta$ | $c_{ph}$ [km/s] peak/node/trough | $\lambda$ [km] | $\alpha = 2\pi R_0/\lambda$ | $c_T$ [km/s] |
|---|---|---|---|---|
| 0.5 | 8.4/8.0/7.7 | 400 | 0.79 | 8.4 |
| 1 | 7.6/7.0/6.8 | 350 | 0.88 | 7.4 |
| 2 | 6.5/6.1/6.0 | 305 | 1.01 | 6.2 |
| 5 | 4.6/4.7/4.8 | 235 | 1.32 | 4.4 |
| 10 | 3.4/3.4/3.4 | 170 | 1.82 | 3.3 |



**Fig. 12.** Mode conversion $M_z$ as a function of dimensionless time for different $\beta$. Mode conversion for the inner cylinder is marked by 'i' and for the outer region labeled by 'o'. $\beta = 1$ cases are shown dashed, $\beta = 0.1$ dash-dotted.

can be treated in a similar manner as the damping rate by leakage before. A suitable quantity describing the mode conversion is given by

$$M_z(t) = \frac{\langle E_{k,z}^i \rangle}{\langle E_k^i \rangle}, \qquad (24)$$

that is, the ratio of the kinetic energy put into $v_z$-motion relative to the total kinetic energy, both measured inside the tube. We remark, that it is also possible to define a quantity describing the amount of kinetic energy stored in internal motions in $y$-direction. However, this effect is found to be small compared with $M_z$.

Fig. 12 shows $M_z$ as a function of the dimensionless time $t/P$ with $\beta$ as a parameter. For $\beta \gtrsim 1$ at $t_{end}$, $M_z$ is roughly constant, yielding a value of $\approx 0.4$. Thus, almost half of the total kinetic energy is fed into longitudinal motions. Comparable calculations using the thin flux tube approximation provide much lower conversion rates (Ulmschneider et al. 1991). For $\beta \lesssim 1$, $M_z$ increases, reaching a value $\approx 0.9$ for the $\beta = 0.1$ tube. However, the low $\beta$ cases have to be considered with reservation because first the condition $t >> P$ is not satisfied and second we suspect that these cases show severe switch-on effects, where a major fraction of the longitudinal kinetic energy here comes from the strong surface feature mentioned above.

To demonstrate that for decreasing $\beta$ an increasingly amount of longitudinal mode conversion comes from the region near the tube boundary, we have devided the tube in an inner cylinder given by $R < 0.8R_0$ and an outer region $0.8R_0 < R < R_0$. For both regions, $M_z$ is calculated separately and shown in Fig. 12 for the cases $\beta = 1$ (dashed lines) and $\beta = 0.1$ (dash-dotted lines). The results for the inner cylinder are denoted by an 'i', those for the outer region by an 'o', respectively. Clearly, mode conversion in the $\beta = 0.1$ tube is dominated by the dynamics near the boundary while a significant fraction of mode conversion results from the inner part in the case $\beta = 1$. This fraction is even higher for the $\beta = 10$ case not shown in Fig. 12.

## 5. Conclusions

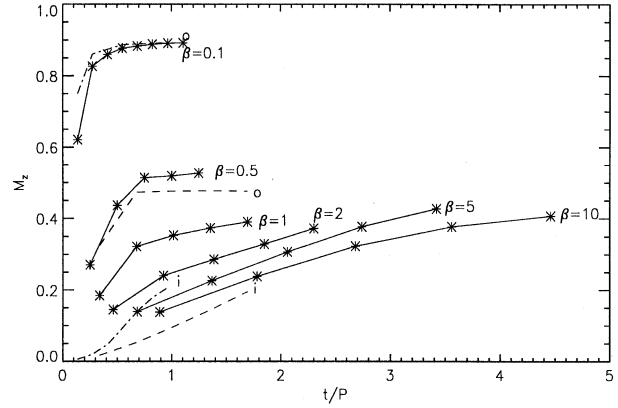We performed adiabatic time-dependent fully compressible 3D magnetohydrodynamic computations in a magnetic flux tube, embedded in a nonmagnetic non-gravitational homogenous atmosphere. High spatial resolution (permitting ca. 300 grid points over the cross section of the tube) was obtained by the application of a multiple nested grid strategy. Tubes of various field strengths $B_z$, where the plasma $\beta = 8\pi p/B_z^2$ varied from 0.1 to 10, were investigated. We considered purely transverse excitation by shaking sinusoidally the tube and its surroundings at the bottom of the atmosphere. Similar velocity amplitudes ($\hat{v} = 2$ km/s) and shaking periods ($P = 50$ s) were used in all computations. From our calculations we draw the following conclusions.

1. In all cases ($\beta = 0.1$ to 10) the swaying tube generated external acoustic waves with a characteristic geometrical pattern resulting from swaying purely in x-direction and from the fact that the external acoustic wave is excited only by the tube and not by the external boundary condition. Low $\beta$ tubes, because of their greater rigidity cause greater external velocity fluctuations.

2. Inside the tube various kinds of longitudinal body waves and a transverse body wave as well as surface waves were found. While a weak sausage-type body wave of twice the frequency of the transverse body wave was detected, a very important result of our computations is the appearance of a non-axisymmetric longitudinal body wave which does not derive from magnetic tension forces, but is due to an inertial pile-up effect inside the tube produced by the transverse motions. This non-axisymmetric longitudinal wave was most pronounced for the $\beta = 10$ tube, where the flow pattern looked like horizontally oriented rolls with an axis perpendicular to the swaying direction.

3. The generated surface waves were more dominant in low $\beta$ tubes, where the tubes are more rigid and interacted more strongly with the external medium.

4. The leakage rates from the flux tube into the external medium range from 0.07 for the $\beta = 10$ to 0.43 for the $\beta = 0.1$ tube. This shows that leakage is an important process particularly for low $\beta$ tubes and should not be ignored in studies of transverse wave propagation.

5. For low $\beta$ tubes the switch-on effects where more pronounced and resulted in surface wave pulses which are caused by the increased rigidity of these tubes.

6. Transverse-longitudinal mode coupling are found to be a very efficient process. Conversion rates up to 90% are found. Thus, mode conversion may be an important mechanism for the heating of flux tubes and consequently for the chromospheric and coronal heating (Hollweg 1982, Sterling & Hollweg 1988). For low $\beta$ tubes essentially the entire mode conversion energy goes into the surface wave.

# References

Cheng J., 1992, A&A 264, 243
Edwin P.M., Roberts B., 1983, *Solar Phys.* 88, 179
Evans C.R., Hawley J.F., 1988, ApJ 307, 337
Ferriz-Mas A., Schüssler M., 1993, Geophys. Astrophys. Fluid Dyn. 72, 209
Goossens M., Hollweg J.V., 1993, *Solar Phys.* 145, 19
Hollweg J.V., 1982, ApJ 257, 345
Huang P., Musielak Z.E., Ulmschneider P., 1995, A&A 297, 579
Huang P., 1995, Ph.D. Thesis, University of Alabama, Huntsville
Huang P., 1996, Phys. Plasmas 3, 2579
Muller R., 1989, in: *Star and Stellar Granulation*, R.J. Rulten, G. Severino, Eds., Kluwer Academic Publ., Dordrecht, p. 101
Muller R., Roudier Th., Vigneau J., Auffret H., 1994, A&A 283, 232
Narain U., Ulmschneider P., 1996, Space Science Review 75, 453
Roberts B., Webb A.R., 1979, *Solar Phys.* 64, 77
Spruit H.C., 1981a, A&A 98, 155
Spruit H.C., 1981b, A&A 102, 129
Spruit H.C., 1982, *Solar Phys.* 75, 3
Stenflo J.O., 1978, Rep. Prog. Phys. 75, 3
Stenuit H., Poedts S., Goossens M., 1993, *Solar Phys.* 147, 13
Sterling A.C., Hollweg J.V., 1988, ApJ 327, 950
Stone J.M., Norman M.L., 1992a, ApJS 80, 753
Stone J.M., Norman M.L., 1992b, ApJS 80, 791
Ulmschneider P., Musielak Z.E., 1997, A&A, in press
Ulmschneider P., Zähringer K., Musielak Z.E., 1991, A&A 241, 625
van Leer B., 1977, JCP 23, 276
Vernazza J.E., Avrett E.H., Löser R., 1981, ApJS 45, 635
Xiao Y., 1988, Ph.D. Thesis, University of Alabama, Huntsville
Ziegler U., Yorke H.W., 1996, CPC, Accepted
Zwaan C., 1978, *Solar Phys.* 60, 213